Computation of turbulence induced vibrations in hard disk drives

Sujit Kirpekar and Prof. David Bogy

Computer Mechanics Laboratory

Department of Mechanical Engineering

University of California at Berkeley

Berkeley, CA 94720

kirpekar@newton.berkeley.edu

April 15, 2004

Contents

1 Introduction **1**

2 CFD Modeling **3**

2.1 The finite volume algorithm 3

2.2 Turbulence Modeling 7

2.2.1 The Kolmogorov microscale of the problem 7

2.2.2 The Smagorinsky model 8

2.2.3 The dynamic model 9

2.2.4 Time discretization 10

3 Structural modeling **11**

3.1 Structural damping 11

3.2 Coupling of the fluid - structure analyses 12

4 Model setup **13**

5 Results **14**

5.1 Vortex dynamics 15

5.2 Global parameters 16

5.3 Drag 16

5.4 Spatial Variation of Pressure 17

5.5 Windage 18

5.6 Vibrational response of the arm 19

5.7 Model Comparison 20

6 Conclusions **22**

7 Tables **26**

8 Figures **26**

List of Figures

1 Front view and Bottom view of CFD model 28

2 Front view and 3D view of eblock arm 29

3 Mode 1: First Bending, 1.252 kHz 29

4 Mode 2: Second Bending, 5.529 kHz 29

5 Mode 3: First Sway, 7.768 kHz 30

6 Mode 4: First Torsion, 9.387 kHz 30

7 Time averaged contours of azimuthal velocity 30

8 Time averaged contours of radial velocity 31

9 Three dimensional view of streamtubes in the wake of the arm 31

10 Orientation of streamtubes relative to the midplane of the model 32

11 Pressure Drag on the arm as a function of time. 32

12 Viscous Drag on the arm as a function of time. 33

13 Frequency Spectrum of the Drag Force. 33

14 Schematic of points where pressure fluctuations are reported. . 34

15 Waterfall plot showing the frequency content of pressure fluctuations at 10 points along the face of the arm. 35

16 Windage loss at disks as a function of time. 36

17 Off-track deflection of arm-tip (nanometers). 36

18 On-track deflection of arm-tip (nanometers). 37

19 Frequency Spectrum of off-track deflections. 38

20 Frequency Spectrum of on-track deflections. 38

21 Out of plane (bending) deflections (nanometers). 39
22 Plot of trajectory of the arm tip in the hortizontal plane. . . . 39
23 Circle (A) and Radius (B-C) along which comparisons of LES models are made 40
24 Comparison of velocities predicted by two models along circle A 41
25 Comparison of velocities predicted by two models along radius B-C 42
26 A comparison of pressure drag predicted by both LES models 43
27 A comparison of windage loss predicted by both LES models . 43
28 A plot of the dynamic coefficient. 44

List of Tables

1 Material Properties of e-block arm 26

2 Natural Frequencies and mode shapes of the e-block arm . . . 27

Abstract

The aim of this study is to numerically study unsteady flows in hard disk drive enclosures by means of large eddy simulation (LES). In particular, the flow between two co-rotating disks obstructed by an e-block arm is simulated. The results of the simulation are used to analyse and describe the topology of the flow, and to characterize the structural response of the e-block arm, which forms the main obstruction to the flow. Global quantities such as the drag on the arm and the windage loss at the disks are reported. Finally, comparisons between 2 different simulations are made to support the assertion that LES is a reliable and accurate method for studying such flows.

1 Introduction

The hard disk drive (HDD) industry is continually faced with demands for higher areal recording densities, faster data transfer rates, and higher reliability. The demand for a higher areal recording density can be met by increasing the track density and/or the linear bit density. Track misregistration (TMR) and flying height modulation (FHM) must both be squeezed into tighter budgets in order to achieve such increases in the track and linear bit densities. On the other hand, the demand for higher data transfer rates has necessitated faster disk rotation speeds. Higher disk speeds increases the turbulence intensity of the flow which results in larger displacements of the arm and suspension.

Early research of Lennemann (1974) on the fluid dynamics of disk drives employed experimental methods using water showed the exsistence of a central rotating laminar core between 2 co-rotating disks. The work of Abrahamson et al. (1989) confirmed the exsistence of three flow regions – the central core, a number of vortical structures and a boundary layer region. Abrahamson et al. (1989) also investigated the effect of the Ekman number on the flow field and concluded that increasing the Ekman number or decreasing the axial separation of the disks increases the number of vortices in the outer region. Humphrey et al. (1995) computationally verified these results and additionally concluded that for high Reynolds numbers, the toroidal vortices "acquire a time varying sinuous shape" and the mid-plane axial vorticity is circumferentially periodic.

In more recent work, Shimizu et al. (2001) performed LES modeling with and without an arm obstruction. Their numerical results correlate well with their experimentally observed disk vibration amplitudes, and by calculating shear stresses on the disk they are able to predict windage loss. In Shimizu et al. (2003) the same authors used LES results to predict air-flow induced vibrations of the head gimbal assembly (HGA). This is one of the first works to use transient LES information to predict displacements of the obstructing structures. Their model, however, is over-simplistic, in the sense that the distributed loading on the structures are approximated by resultant forces acting at certain pre-defined points. It is also unclear how the authors calculate the skin friction drag since they do not mention the integration of wall

shear stress. Tsuda et al. (2003) performed a direct numerical simulation (DNS) and compared their results with experiments. They reported the existence of a three dimensional spiral vortex in the wake of the e-block arm. Tatewaki et al. (2001) performed LES calculations of three obstructed and unobstructed disks and demonstrated the spatial structure of the pressure fluctuations with direct applications to disk flutter.

The current study is also a LES compuation of the flow between two disks with an e-block arm. We draw useful conclusions about the simulation by the use of two different LES models. We also examine the vibration of the structure, and for this we employ a rigorous technique without the use of *ad hoc* simplifications.

2 CFD Modeling

2.1 The finite volume algorithm

Our simulations were performed using the commercial computational fluid dynamics (CFD) software – CFDRC. This software includes an unstructured, polyhedral cell flow solver, an interactive geometry modeling and grid generation system and a post-processing system. The code solves the equations of motion in strong conservation form using the finite volume method. The algorithm uses the well-known SIMPLEC (Semi-Implicit Method for Pressure-Linked Equations: Consistent). A very good description of pressure correction methods is given in Anderson (1995), and the original algorithm is

published in Van doormaal and Raithby (1984). We describe the highlights here.

In solving the integral form of the Navier Stokes equations (momentum) in discretized form, we seek solutions of equations of the form,

$$A_P u_{i,P}^{n+1} + \sum_l A_l u_{i,l}^{n+1} = -\left(\frac{\delta p}{\delta x_i}\right)_P^{n+1} \tag{1}$$

which represents an equation for the velocity components u_i at the point P. The quantities $u_{i,l}$ are the velocity components at the neighbouring grid locations, and the coefficients A_P and A_l are determined by the scheme used to discretize the advective and diffusive terms in the Navier Stokes equations. We use the symbol δ to denote the specific numerical scheme to implement the gradient of pressure (e.g. central differencing). In this report, we use the notation in Ferzige and Peric (2002). Notice that Eqn. 1 is implicit and hence it requires the solution of a large system of non-linear equations. We also note that by choosing an implcit scheme we are not restricted by the CFL-like conditions on the time-step, and the numerical method is assured of unconditional stability in time. In fact, we use a first order (Backward Euler's) implicit method, because of its simplicity. A first order $O(\Delta t)$ accurate scheme is indeed acceptable, since our time step is already restricted by the physics of the flow.

The equation of continuity is represented by,

$$\frac{\delta u_i}{\delta x_i} = 0 \tag{2}$$

The SIMPLEC algorithm is inherently iterative – it uses pressure and velocity data from the previous time-step (or iteration) and corrects it by satifying the continuity and momentum equations. We denote the previous values of velocity and pressure by u^{m*} and p^{m*}, and propose corrections of the form,

$$u^m = u^{m*} + u'; \qquad p^m = p^{m*} + p'; \tag{3}$$

where the subscript i has been dropped for notational convenience. Since u^{m*} from the previous iteration satisfies Eqn. 1 we may write,

$$u_{i,P}^{m*} = \frac{-\sum_l A_l u_l^{m*}}{A_P} - \frac{1}{A_P}\left(\frac{\delta p}{\delta x_i}\right)^{m*} \tag{4}$$

or

$$u_{i,P}^{m*} = \tilde{u}_i^{m*} - \frac{1}{A_P}\left(\frac{\delta p}{\delta x_i}\right)^{m*} \tag{5}$$

where,

$$\tilde{u}_i^{m*} = \frac{-\sum_l A_l u_l^{m*}}{A_P} \tag{6}$$

Taking the divergence of Eqn. 5 we obtain the following Poisson equation

for the pressure correction,

$$\frac{\delta}{\delta x_i}\left(\frac{1}{A_P}\frac{\delta p'}{\delta x_i}\right) = \frac{\delta}{\delta x_i}\left(\tilde{u}'_{i,P}\right) + \frac{\delta}{\delta x_i}\left(u^{m*}_{i,P}\right) \tag{7}$$

Since the term $\tilde{u}'_{i,P}$ is still unknown we approximate it by the following equation: (which forms the basic assumption of the SIMPLEC Method)

$$\tilde{u}'_{i,P} = -u'_{i,P}\frac{\sum_l A_l}{A_P} \tag{8}$$

This gives the final equation to solve, so that the pressure correction satifies the divergence condition,

$$\frac{\delta}{\delta x_i}\left(\frac{\rho}{A_P + \sum_l A_l}\frac{\delta p'}{\delta x_i}\right) = \frac{\delta}{\delta x_i}\left(\rho u^{m*}_{i,P}\right) \tag{9}$$

Once the pressure correction is obtained, it is used to solve the momentum equations (Eqn. 1) to obtain the corrected velocities. This procedure is continued until the corrections obtained are sufficiently small with each iteration. In our simulation, the criterion for convergence was maintained at 10^{-4}.

To evaluate the fluxes at the cell boundaries (for integration of the convective terms) from the variable values at the cell center, we use second order central differencing. However to increase the stability of such a scheme in an inherently iterative solver, we "blend" it with a first order upwind differencing scheme. The contribution of the upwinding scheme was limited to no

more 10%.

2.2 Turbulence Modeling

2.2.1 The Kolmogorov microscale of the problem

For the problem of turbulence it is not practical to compute the Navier Stokes equations directly, because of their complexity. The Kolmogorov microscale may be computed approximately as,

$$\eta = \left(\frac{\nu^3}{\varepsilon}\right)^{1/4} = O(10^{-5})m \tag{10}$$

and this value implies that our simulation would need approximately $O(10^{10})$ cells in a typical 3D domain. Here, η = Kolmogorov's scale, ν = Molecular viscosity and ε = Disspiation rate. The same result could be obtained (approximately) by realizing that the number of grid cells in a direct simulation is on the order of $Re^{9/4}$. We define the Re of the flow using the disk separation: $Re = \omega Rh/\nu$, where R is the disk radius, ω is the angular velocity and h is the disk-to-disk separation. This is often refered to as the *tip-based Reynolds number* because it uses the outer radius R. From using these grid size estimates, we conclude that a direct simulation would be impossible using our current computer workstations. Therefore we use Large Eddy Simulation (LES). To gain more insight into the CFD solution of the problem, we performed simulations with two different LES models and compare their results. These models are described briefly below. We assume the

reader is familiar with the LES technique; For an introduction to the practice of LES, we refer the reader to Ferziger (1983), Ferziger (1996) and Rogallo and Moin (1984).

2.2.2 The Smagorinsky model

In large eddy simulation the effect of large scales is directly computed by a filtered version of the Navier Stokes equations, while the small scales are modeled. Since small scales tend to be more isotropic than large ones, it is usually acceptable to parameterize them using an eddy viscosity assumption. In the well known Smagorinsky model (Smagorinsky, 1963) the eddy viscosity is obtained by application of the equilibirum hypothesis, i.e. by assuming that small scales are in equilibrium due to the simultaneous cascade and dissipation of energy. This gives an expression of the form,

$$\nu_T = (C_s \Delta)^2 |\bar{S}| \tag{11}$$

where Δ is the filter width, C_s is Smagorinsky's constant, $|\bar{S}|$ is the magnitude of the strain rate tensor,

$$\bar{S_{ij}} = \frac{1}{2}\left(\frac{\partial \bar{u}_i}{\partial x_j} + \frac{\partial \bar{u}_j}{\partial x_i}\right)$$

and $\bar{u}_i$ is the resolved velocity.

Unfortunately there is no common agreement on the value of C_s, which is determined empirically. The more complicated the flow gets, the more

difficult it is to predict the model constant C_s, and no such value is known for separated shear flows with curved streamlines, as in our case. Additionally, the model must rely on *ad hoc* methods to extrapolate sub grid scale (SGS) shear stresses near the wall. The CFDRC simulation software uses the well known Van Driest damping function (Van Driest, 1956) to locally extrapolate eddy viscosity to the wall. The behaviour of the model at the wall is especially important to our simulation since we need to calculate the shear stress at the wall (which will helps us determine the "windage" loss). And finally, since the model constant is fixed, the model does not allow energy flow from small scales to large scales which according to Germano et al. (1991) can be significant, and it produces excessive disspation of large scale fluctuations.

2.2.3 The dynamic model

The dynamic SGS model due to Germano et al. (1991) is based on the same eddy viscosity model as above, except that the model constant is computed dynamically as the calculation progresses. By filtering the equations of motion using two filters of different filter widths, it is possible to derive an algebraic expression for the model constant. These are often called sub-grid and sub-test filters. This, however, leads to 5 equations for a single model constant, and the error in the eddy viscosity assumption is minimized by the use of a least squares technique as explained in Lilly (1992). This proposed modification to the dynamic model makes it a more appropriate candidate for universal application, than the Smagorinsky's model. The mathematical

formulation of the technique is lucidly discussed in Lilly (1992).

The advantages using this model are multifold: Firstly, the SGS stress vanishes at the walls and shows the correct aymptotic behaviour (y^3) near the walls. This eliminates the use of wall functions in the model. Also, since the model constant may be locally negative, the model allows for reverse energy cascade, i.e. backscatter. The only parameter that needs to be supplied is the ratio of the sub-grid to the sub-test filter widths. We use the optimized value of 0.5 as presented in Germano et al. (1991).

2.2.4 Time discretization

The time step is chosen so that numerical stability is assured and the turbulent motions are accurately resolved in time. We ensure that the time-step is smaller than the time scale of the smallest resolved scale of motion. This is given by,

$$\tau = \frac{\Delta x}{U} \tag{12}$$

where Δx is the grid spacing and U is the mean (outer) velocity at that position. Considering this condition we choose a time-step of 10^{-5}. We also note, at this point, that the frequencies of oscillations of the structures in a disk drive have experimetally been determined to be on the order of a few kHz, hence such a small time step is indeed necessary to resolve the dynamics of the flow.

3 Structural modeling

To compute the response of the structure obstructing the flow, we employ a finite element stress solver module included in the CFDRC software that can be directly coupled to the flow solver. The equations of structural mechanics are solved in finite element form as derived from the principal of virtual work. For each element, displacements are defined at the nodes and are obtained within the element in the usual manner, by interpolation from the nodal values using shape functions.

3.1 Structural damping

To treat structural damping in the e-block arm we use the simple Rayleigh damping (proportional damping) method. By assuming,

$$\mathbf{C} = \alpha\mathbf{M} + \beta\mathbf{K} \tag{13}$$

where $\mathbf{M}$, $\mathbf{C}$ and $\mathbf{K}$ are the mass, damping and stiffness matrices respectively, we get the following equation for each degree of freedom of the system,

$$\xi_i = \frac{1}{2}\left(\frac{\alpha}{\omega_i} + \beta\omega_i\right) \tag{14}$$

where ξ_i is the damping ratio and ω_i is the natural frequency of the ith mode. As explained in Cook et al. (1989), such a formulation permits us

to choose the amount of damping for two specific frequencies to determine the two coefficients, α and β. In our particular case we choose the damping at the first and tenth modes of vibration of the structure to 5% of critical damping. This effectively guarantees that the damping in the spectrum of interest (first ten modes, 1-40 kHz) will be below 5%, and vibration modes outside this range will be strongly damped out.

3.2 Coupling of the fluid - structure analyses

On completion of each time-step by the flow solver, the pressure data (normal loading) and shear stress at the wall (tangential loading) are passed on to the stress solver. These force boundary conditions are implemented on a face by face basis, without the use of simplifying assumptions. To the authors' knowledge this is the first study of the hard disk drive problem to rigorously couple the flow-structure problems. The FE stress solver thus determines the response of the structure as the simulation progresses. We note that the deflections of the e-block arm are usually very small compared to the grid size in the vicinity of the arm. Hence, we do not need to re-mesh the domain surrounding the arm, although the displacement of the wall is finite. In this sense, the problem is coupled in one way only: the fluid flow affects the structural vibration but not vice versa.

4 Model setup

Our model consists of two 3.5" disks rotating in a fixed, closed enclosure. The disk to shroud radial clearance is 2 mm and this clearance is closed by flat walls at the top and bottom. The disk rotation speed is 10,000 rpm. Each time step of 10^{-5} seconds corresponds to 0.6 degrees of rotation of the disks. The calculation is carried out for 6 revolutions, i.e. 3600 time steps. Theoretically, our simulations are able to resolve a maximum frequency of 50 kHz. However, we limit this to 10 kHz from a data storage point of view.

The model was meshed using an unstructured grid with 395,000 cells. The e-block arm used in the simulation matches geometrically with experimental work done previously by Gross et al. (2002). Fig. 1 shows the front view and bottom view of the CFD model, and a 3-dimensional view of the e-block arm is shown in Fig. 2. Table 1 gives the material properties used for the e-block arm. The e-block is treated as a cantilever with its pivot fixed, and it is placed symmetrically at the midplane between the two disks. As shwon in Fig. 1, the arm is tilted at 32 degrees to the vertical axis, representative of the configuration during read-write operations.

To begin, a modal analysis is performed on the e-block arm to estimate its natural frequencies of vibration. The natural frequencies and mode shapes are listed in Table 2. The first four modes are also shown in Fig. 3 - Fig. 6. Of particular interest to the current problem are the sway modes, which contribute the most to the off-track displacement, while the lower bending

modes contribute largely to the on-track discplacement. We note that off-track is defined as orthogonal to the axis of symmetry of the e-block arm, while on-track is along the axis of the arm.

The LES simulation is initialized from a steady state RANS (Reynolds Averaged Navier Stokes) solution, using the standard $k - \epsilon$ model. To this solution, we add 5% random fluctuations to the velocities, to perturb the base flow. This implies that for the initial condition, the flow field is assumed to be in steady state with the rotating disks, with small pertubations from the mean.

5 Results

All of the results presented in this section refer to the simulation using the dynamic LES model, unless otherwise noted. We conclude our discussion in Sec. 5.7 by comparing the results from the two LES models.

The flow inside a disk drive casing is very complex and involves regions of mostly transitional and turbulent flows. For the configuration in our simulations the flow field near the center of the rotating disks remained transitional, while most of the other regions – including the sheared region at the shroud and the wake – remained largely turbulent.

The flow displays a strong stagnation zone near the leading edge of the arm. The top and bottom surfaces of the arm contain regions of unsteady separation and reattachment which results in the formation of coherent struc-

tures, particularly in the wake of the arm. The wake itself is very complex showing regions of shear and the presence of intense vortices that are continually being transported due to the shearing effect of the rotating walls at the top and bottom. Due to the lack of symmetry of the arm with respect to the incoming flow there appears to be no strict periodicity in the shedding of vortices.

Fig. 7 and Fig. 8 show the time averaged contour plots of the azimuthal and radial velocities, respectively, in the mid plane of the model, averaged after 5 revolutions of the disk. The figures show a largely uniform flow field in about the 3/4 portion of the drive upstream of the arm. The wake region contains a more irregular flow topology. Interestingly there is a small region of flow reversal, near the hub, just upstream of the arm. This flow reversal is probably due to the adverse pressure gradient (the flow stagnates at the arm). The radial contours show a strong inflow in the wake of the arm; this is primarily due to the constraining geometry and the disk rotation.

5.1 Vortex dynamics

Fig. 9 shows a three dimensional view of instantenous streamtubes in the region of the wake behind the arm. They are color-coded (for contrast) according to the azimuthal velocity. Fig. 10 shows the orientation of these tubes with respect to the midplane. Additionally the midplane is colored to reflect the axial velocity of the flow. These figures demonstrate the orientation of vortical structures shed by the arm, whose axes are oriented at an

angle to the arm. This is most likely due to the "forcing" of the disks, and results in an orientation that is different compared to the wake of a regular cylinder. Eddies are typically generated from every sharp edge of the arm and transported downstream by the Couette type flow. These structures are coherent and persistent; viscous dissipation does not cause them to be dissipated completely before they approach the arm after being transported to its upstream side.

5.2 Global parameters

A commonly reported non-dimensional frequency of the flow is the Strouhal Number. We do not report this number here, since our observations show that eddies are shed from more than one point along the face of the arm. Additionally, these points have different mean velocities of the upstream flow which causes the difficulty in reporting a *global* Strouhal Number. We also note that this quantity is not a significant test of the quality of the simulation as noted in Rodi et al. (1997)

5.3 Drag

Fig. 11 and Fig. 12 show the pressure drag and the viscous drag on the arm as a function of time. We define drag as the net resultant force acting in a direction perpendicular to the axis of symmetry of the arm. These have been obtained by integrating the pressure and shear stress on the area of the arm

using,

$$F_p = \int_{\partial S_1} p \, dA; \qquad F_\tau = \int_{\partial S_2} \tau_w \, dA \tag{15}$$

where ∂S_1 denotes the surfaces of the arm normal to the general upstream flow direction (the thin edges of the arm including the holes), p denotes the pressure acting on these faces, ∂S_2 denotes the surfaces of the arm tangent to the general upstream flow direction (the top and bottom faces of the arm) and τ_w is the shear stress acting on these faces (∂S_2). We note that the viscous drag (or the skin friction drag) is two orders of magnitude smaller than the pressure drag, and hence the corresponding contribution of the pressure drag to the vibration of the arm is significantly higher.

Fig. 13 shows the frequency spectrum of the total drag. We see that the power of the spectrum is concentrated in the low frequency (0 - 3 kHz) range, and the higher frequency part of the spectrum is more uniform. This implies that we can (numerically) expect a low frequency forcing of the e-block arm by the flow.

5.4 Spatial Variation of Pressure

Given that pressure contributes the most to the vibrations of the arm, we discuss the pressure fluctuations in the flow field along the leading edge face of the arm. In particular, we note the pressure at ten points on the leading edge face of the arm as shown by the small dots in Fig. 14. The points

are numbered so that they start from 1 at the tip of the arm, and go to 10 at the fixed pivot of the arm. Fig. 15 shows a waterfall plot, where each line denotes the frequency spectrum of pressure fluctuation at that point. From this figure we again note that the pressure fluctuations are rich in the low frequency range. It is of interest to note that point #9 displays a significantly higher amplitude (of the spectrum) in the low frequency range than its neighbours. This is most likely due to the fact that the upstream incoming velocity is the highest at this point, and this results in a large pressure rise as the flow stagnates at the face of the arm.

5.5 Windage

Finally, we also calculate the windage loss at the disks. This refers to the power required by the motor to rotate the disks at 10,000 rpm due to viscous effects. This quantity may be easily calculated as,

$$W = \int_{\partial D} \tau \mathbf{u}|_{\text{wall}} \, dA = \int_{\partial D} \tau_{\phi z} u_{\phi}|_{\text{wall}} \, dA \tag{16}$$

Fig. 16 shows a time history of the windage loss. We note that this estimate of windage considers only 1 face of each of the 2 rotating disks. In an actual drive windage is due to power lost on both faces of each rotating disk. We also note that we do not include the power lost at the arm due to shear.

5.6 Vibrational response of the arm

We decompose the vibrational response of the arm into two components: the on-track displacements , lying along the axis of the arm, and the off-track displacements, lying orthogonal to the axis of the arm. To study the response of the arm to the flow field we analyse the displacement of the structure at its tip on its lower face. This is the region where the suspension is attached in a real drive.

Fig. 17 and Fig. 18 show the displacements of the end of the arm in the off-track and on-track directions respectively. Fig. 19 and Fig. 20 show the corresponding frequency spectra. From the figures, we conclude that the off-track amplitude is limited to about 2.2 nm peak-to-peak, with a mean at about 2.2 nm also. The on-track vibration is significantly greater, with a peak to peak amplitude of about 5.2 nm, with a mean at about 2 nm. We conclude that the response of the arm in the on-track direction is larger due to its lower stiffness in bending. Since the arm is modelled here as a cantilever, its lowest stiffness is in bending, and this causes relatively large bending vibrations (out of plane vibrations) as shown in Fig. 21. Large on-track displacements are simply a consequence of the bending.

The frequency spectra of the vibrations correlate very well with the modal analysis. In Fig. 19 peaks are seen at 5.785 kHz (very close to the second bending mode), 7.621 kHz (first torsional mode) and a large peak at 8.901 kHz (close to the first sway mode). In the on-track spectrum, a large portion of the power is concentrated in the region close to the 1.252 kHz first bending

mode, implying that the dominating frequency of oscillation corresponds to the first bending mode. Additionally, the second bending, first torsion and first sway modes are also evident.

For a more physical insight into the vibrations, we plot the trajectory of the point under consideration on the x-y plane in Fig. 22, where the large dot represents its original undeflected position.

We conclude this discussion by noting that the vibrations of the e-block arm are primarily dominated by the first bending mode. In practice, the boundary conditions for the drive level components are different, given that a suspension and slider is attahced to the end of the arm. However, our results showing the off-track component should carry over to realistic drive configurations, which will be included in the follow-on study.

5.7 Model Comparison

Fig. 23 shows the radial line BC and a circle A along which the results of the two LES models are compared. Fig. 24 shows the detailed comparisons along these lines at the midplane of the drive. The figures show plots of the midplane azimuthal, radial and axial components of velocity $(\bar{u}_{phi}, \bar{u}_r, \bar{u}_z)$ at a radius of 20 mm (circle A) as a function of the polar angle. These figures are accompanied by plots of corresponding fluctuations (u'_{phi}, u'_r, u'_z). All quantities are time averaged over five revolutions of the disk. We notice that the radial and azimuthal velocities agree quite well between the two LES models, (which form the mean flow) and so do their fluctuations. However,

the axial components, which reflect the three dimensionality of the flow, do not show much similarity. Since this is a secondary (or perturbation) flow, $O(\bar{u}_z) \equiv O(u'_z)$, we do not expect much agreement of these quantities between the models.

One of the claims of the dynamic model is that it maintains the dissipation at more physical values. To examine this, we plot in Fig. 25 the three components of velocity and their fluctuations at an upstream location (along radius B-C, in Fig. 23) as a function of the radius (again, averaged over 5 revolutions). Again, the velocity components of the radial and azimuthal flow agree well, but there is less agreement in the axial component. This indicates that the two models predict comparable flow topologies when averaged over time, but the dynamics of the flow may differ.

To examine other quantities we plot the pressure drag and the windage for each model in Fig. 26 and Fig. 27 respectively. We observe that the dynamic model predicts higher drag (on the e-block arm) and a higher windage on the disks. The reason for this is that the dynamic model is better able to resolve near-wall turbulence than the Smagorinsky wall functions. We also note that the frequency spectra for drag did not differ significantly between the two models, and hence they are not plotted again here (see Fig. 13). Additionally, the frequency spectra for pressure fluctuations at the e-block arm face do not differ significantly, (see Fig. 15). We conclude from this, that in computing the unsteady dynamics of the flow, the models do not differ significantly.

Lastly, we plot in Fig. 28 the model constant determined by the dynamic model over the entire domain. In the norm, the constant compares well with the constant used by the Smagorinsky's model ($C_s = 0.1$), but clearly the Smagorinsky's model fails to capture any local variation of the model parameter. Since the dynamic model does not predict any negative model parameter values, its fails to predict any backscatter. However this may not be the case if the numerical experiments were performed with successively smaller grids as suggested in Rodi et al. (1997), but this is beyond the scope of our current analysis.

6 Conclusions

Large Eddy Simulation is a useful tool for studing flows in disk drives. Our simulations provide a rich data in terms of pressure and velocities. We have also been successful in integrating the flow and stress solvers, and the strucural response results agree quite well with the modal analysis.

In terms of the flow topology, we observe a highly complicated shear flow with aperiodic vortex shedding in the wake of the arm. The turbulent eddies are not dissipated completely by the time they complete one revolution. The pressure fluctuations are rich in the low frequency (0-3 kHz) range and act as low frequency excitations to the structures. The pressure drag on the arm is two orders in magnitude larger than the viscous drag.

In terms of the response of the arm to the flow – the structure vibrates

at frequencies corresponding to its first few modes. Due to the nature of the model (i.e. the arm being modeled as a cantilever) the arm shows relatively large vibrations in bending, which in turn contribute to the on-track displacement. The vibrations that are more important to designers, (i.e. off-track) correspond closely to the first sway mode, which in our case has a frequency of 9.3 kHz. They display a mean displacement of about 2.19 nm and a peak-to-peak amplitude of 2.18 nm.

On the topic of comparison of the two turbulence models, we note that the complicated geometry of the disk drive enclosure does not lend itself to fundamental turbulence analysis, e.g. kinetic energy spectra. However by comparing a few quantities we are able to conclude that the two models are in good agreement when comparing average flow quantities. It is often observed that instantaneous values of primitive variables are fairly different but the time scale of variation (and hence the frequency spectra) are remarkably similar between the two LES models. The primary advantage of using the dynamic model is that it does not use *ad hoc* methods to extrapolate stresses at the wall – hence it may offer more realistic values for wall shear stress and pressure.

In future stduies we will include the suspension and read-write heads. Our analysis will still be incomplete due to the lack of any experimental validation. We believe that experimental data coupled with our numerical simulations will lead to a reliable and accurate understanding of the effects of air-turbulence on the dynamics of hard disk drives.

References

E. Lennemann. Aerodynamic aspects of disk files. *IBM J. Res. Develop*, pages 480–488, 1974.

S. D. Abrahamson, John Eaton, and D. J. Koga. The flow between shrouded co-rotaing disks. *Physics of Fluids*, 1(2):241–251, 1989.

J. A. C. Humphrey, C. A. Schuler, and D. R. Webster. Unsteady laminar flow between a pair of disks corotating in a fixed cylindrical enclosure. *Physics of Fluids*, 7(6):1225–1240, 1995.

H. Shimizu, M. Tokuyama, S. Imai, S. Nakamura, and K. Sakai. Study of aerodynamic characteristics in hard disk drives by numerical simulation. *IEEE Transcations on Magnetics*, 37(2):831–836, 2001.

H. Shimizu, T. Shimizu, M. Tokuyama, H. Masuda, and S. Nakamura. Numerical simulation of positioning error caused by air-flow-induced vibration of head gimbals assembly in hard disk drive. *IEEE Transcations on Magnetics*, 39(2):806–811, 2003.

N. Tsuda, H. Kobutera, M. Tatewaki, S. Noda, M. Hashiguchi, and T. Maruyama. Unsteady analysis and experimental verification of the aerodynamic vibration mechanism of hdd arms. *IEEE Transcations on Magnetics*, 39(2):819–825, 2003.

M. Tatewaki, N. Tsuda, and T. Maruyama. A numerical simulation of unsteady airflow in hdds. *FUJITSU Sci. Tech. J.*, 37(2):227–235, 2001.

J. D. Jr. Anderson. *Computational Fluid Dynamics*. McGraw-Hill, 1995.

J. P. Van doormaal and G. D. Raithby. Enhancements of the simple method incompressible fluid flows. *Numerical Heat Transfer*, 7:147–163, 1984.

J. H. Ferzige and M. Peric. *Computational Methods for Fluid Dynamics*. Springer, 2002.

J. H. Ferziger. *Higher level simulations of turbulent flows in Compuational methods for turbulent, transonic and viscous flows*. 1983.

J. H. Ferziger. *Simulation and modeling of turbulent flows*. Cambridge University Press, 1996.

R. S. Rogallo and P. Moin. Numerical simulation of turbulent flows. *Annual Review of fluid mechanics*, 16:99–137, 1984.

J. Smagorinsky. General circulation experiments with the primitive equations, i. the basic experiment. *Monthly Weather Review*, 91:99–164, 1963.

E. R. Van Driest. On turbulent flow near a wall. *Journal of Aero. Science*, 23:1007–1011, 1956.

M. Germano, U. Piomelli, P. Moin, and W. H. Cabot. A dynamic sub-grid scale eddy viscosity model. *Physics of Fluids*, A(3):1760–1765, 1991.

D. K. Lilly. A proposed modification of the germano subgrid scale closure method. *Physics of Fluids*, A(4):633–635, 1992.

R. D. Cook, D. S. Malkus, and M. E. Plesha. *Concepts and Applications of Finite Element Analysis*. John Wiley and Sons, third edition, 1989.

Hany M. Gross, Toru Watanabe, D. B. Bogy, and O. Savas. The effects of e-block arm thickness on the airflow past the head stack assembly in a modeled hard disk drive. *CML Technical Report*, 2002.

W. Rodi, J. H. Ferziger, M. Breuer, and M. Pourquie. Status of large eddy simulation: Results of a workshop. *ASME Journal of Fluids Engineering*, 119:248–261, 1997.

7 Tables

Table 1: Material Properties of e-block arm

Young's Modulus	69 GPa
Density	2710 kg/m^3
Poisson's Ratio	0.33

8 Figures

Table 2: Natural Frequencies and mode shapes of the e-block arm

Mode Number	Natural Frequency (kHz)	Mode Shape
1	1.252	First Bending
2	5.529	Second Bending
3	7.768	First Torsion
4	9.387	First Sway
5	13.792	Third Bending
6	16.877	Second Torsion
7	24.398	Fourth Bending
8	25.292	Second Sway
9	28.103	Third Torsion
10	40.733	Third Sway

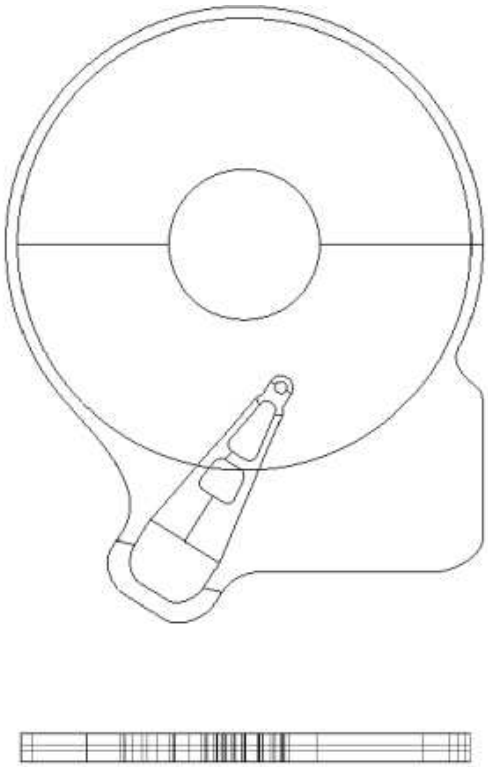

Figure 1: Front view and Bottom view of CFD model

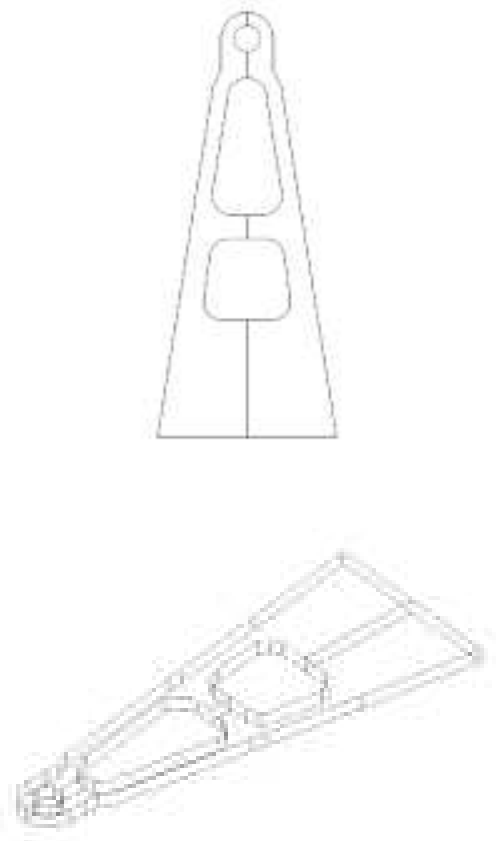

Figure 2: Front view and 3D view of eblock arm

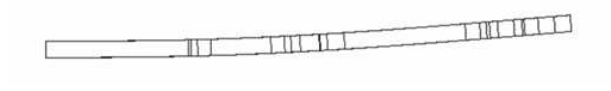

Figure 3: Mode 1: First Bending, 1.252 kHz

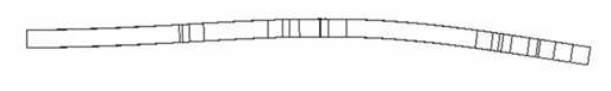

Figure 4: Mode 2: Second Bending, 5.529 kHz

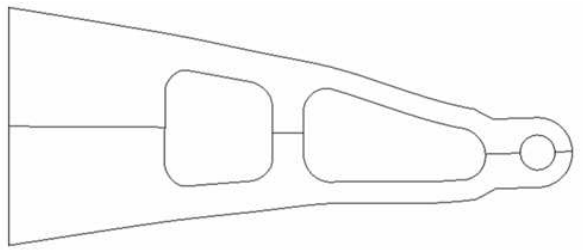

Figure 5: Mode 3: First Sway, 7.768 kHz

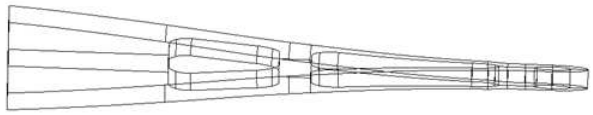

Figure 6: Mode 4: First Torsion, 9.387 kHz

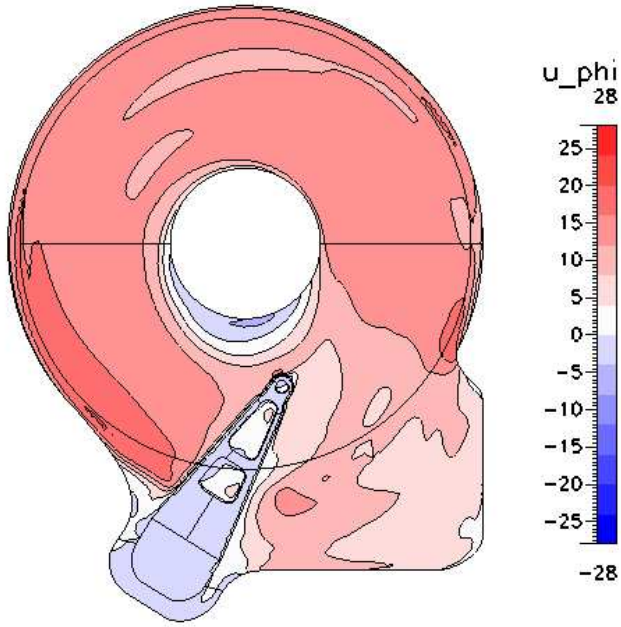

Figure 7: Time averaged contours of azimuthal velocity

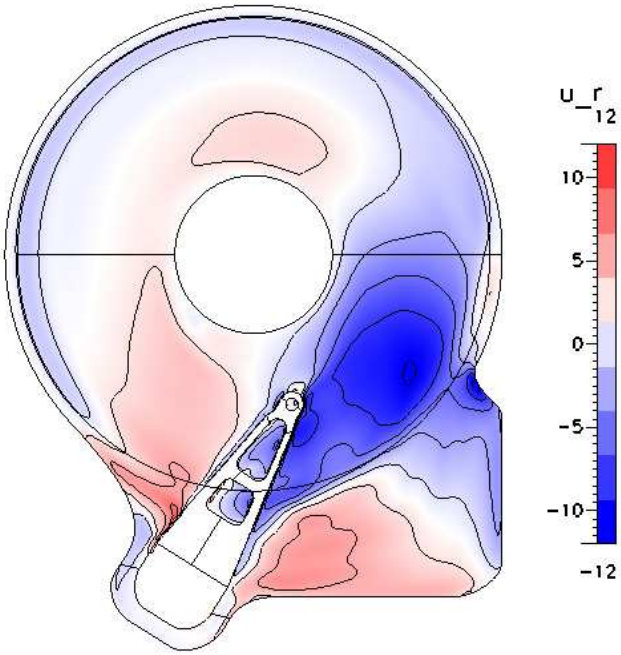

Figure 8: Time averaged contours of radial velocity

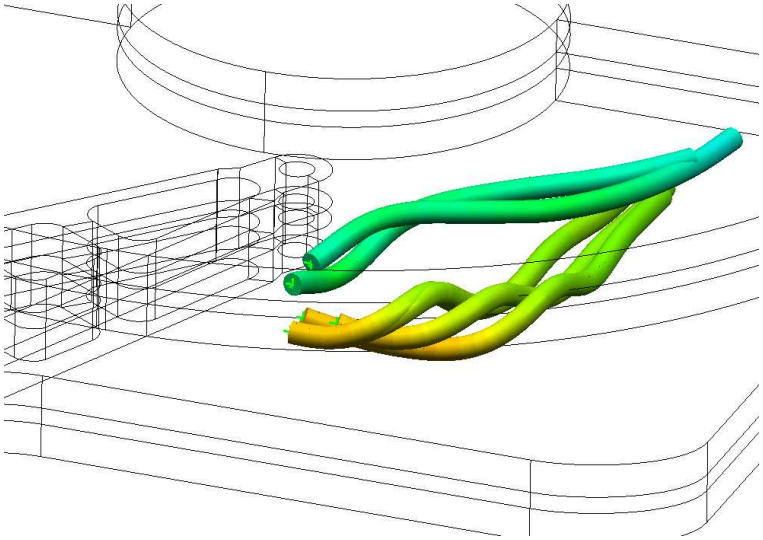

Figure 9: Three dimensional view of streamtubes in the wake of the arm

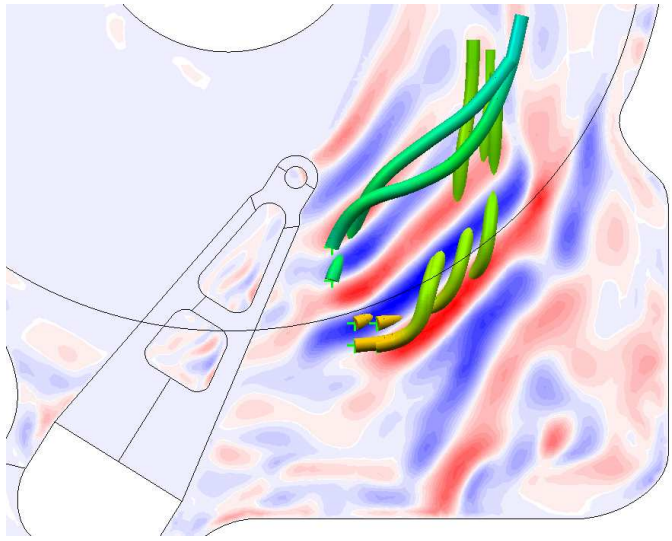

Figure 10: [h] Orientation of streamtubes relative to the midplane of the model

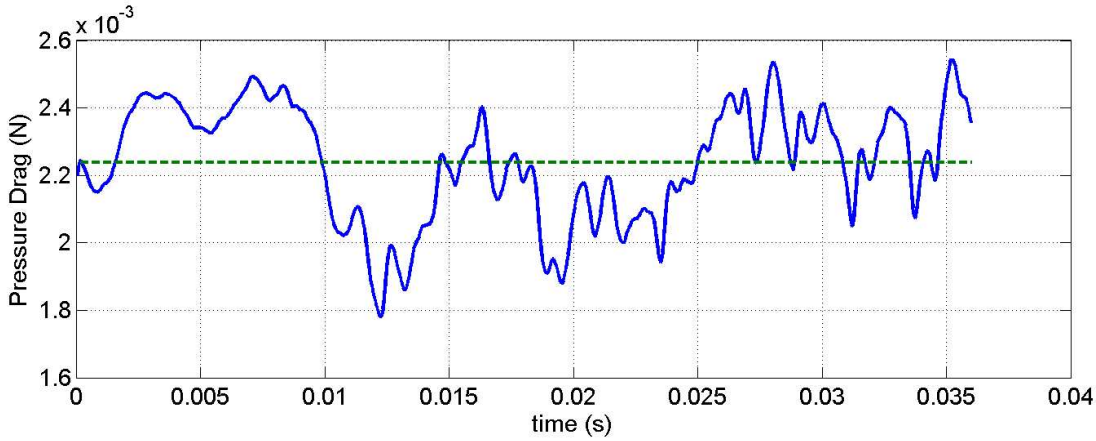

Figure 11: Pressure Drag on the arm as a function of time. The dotted line indicates the mean value

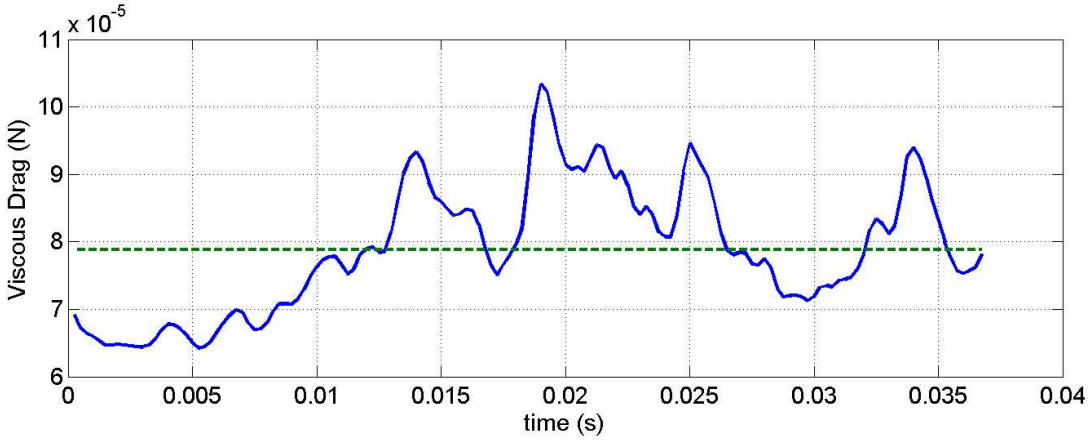

Figure 12: Viscous Drag on the arm as a function of time. The dotted line indicates the mean value

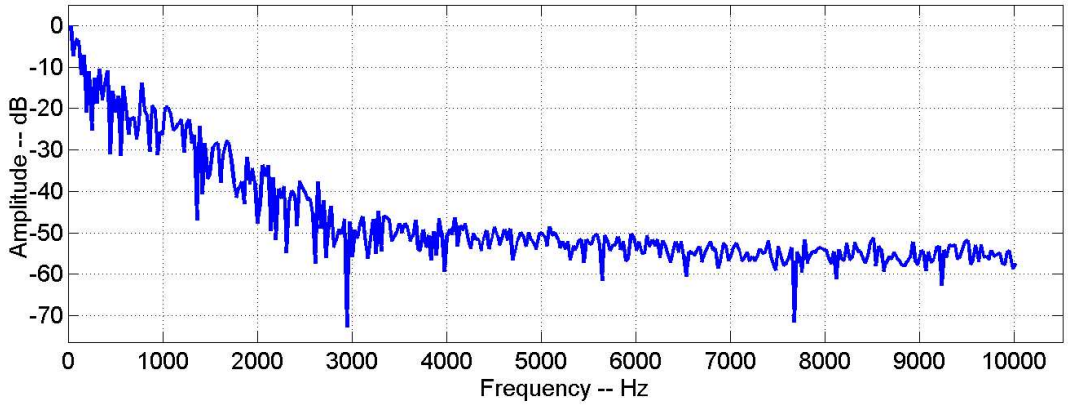

Figure 13: Frequency Spectrum of the Drag Force.

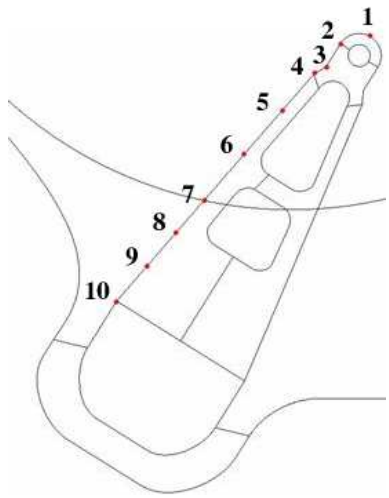

Figure 14: Schematic of points where pressure fluctuations are reported.

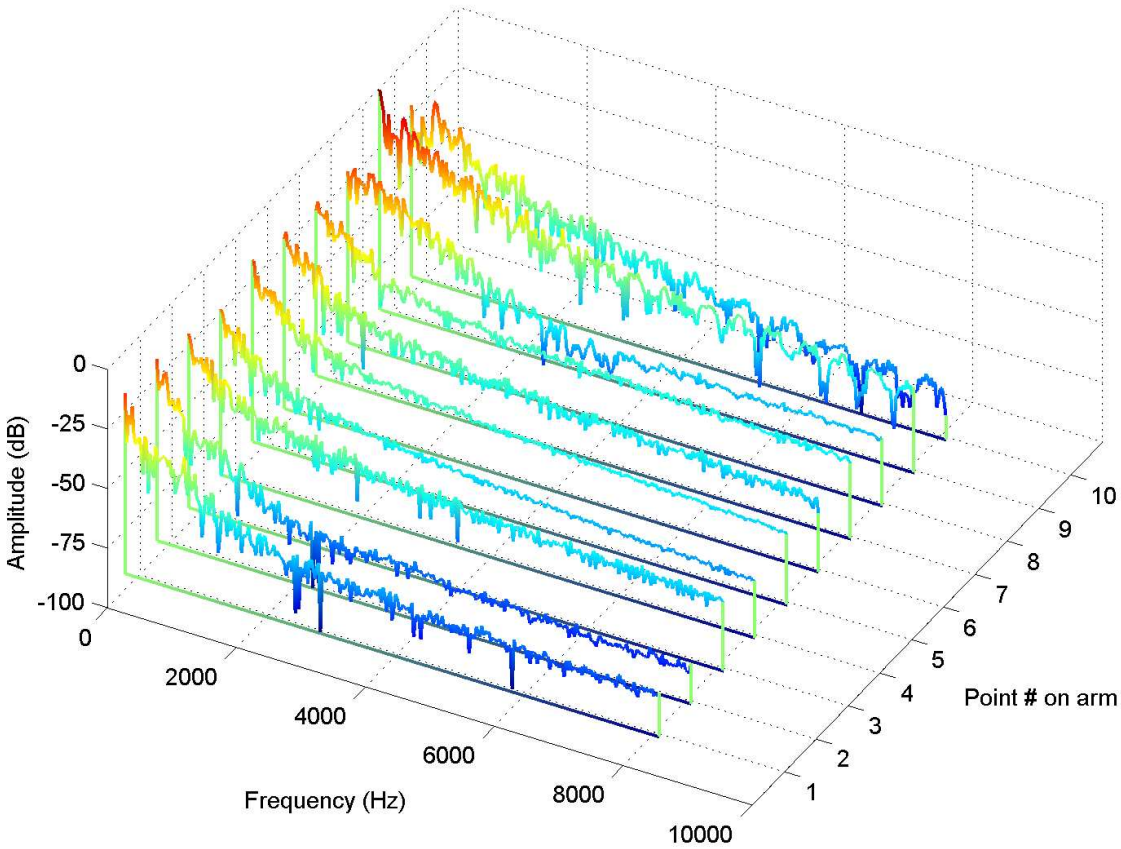

Figure 15: Waterfall plot showing the frequency content of pressure fluctuations at 10 points along the face of the arm.

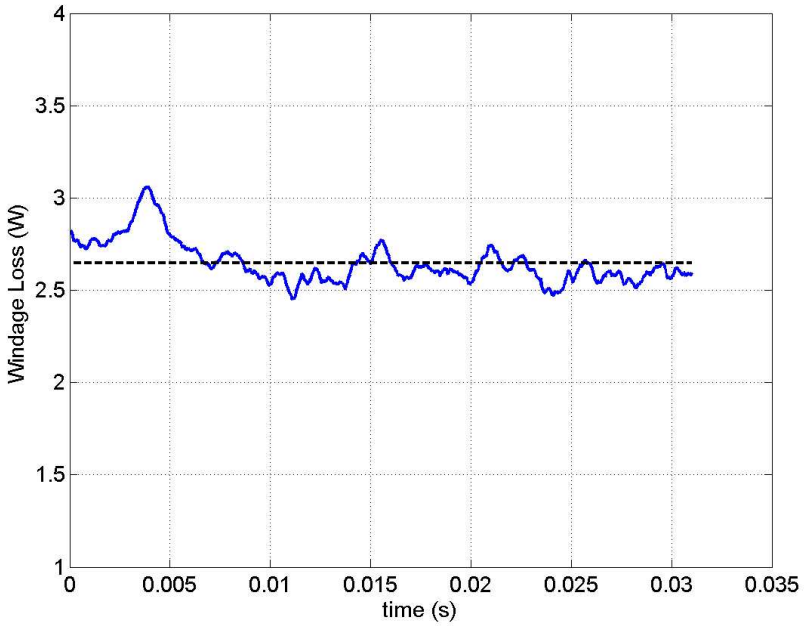

Figure 16: Windage loss at disks as a function of time.

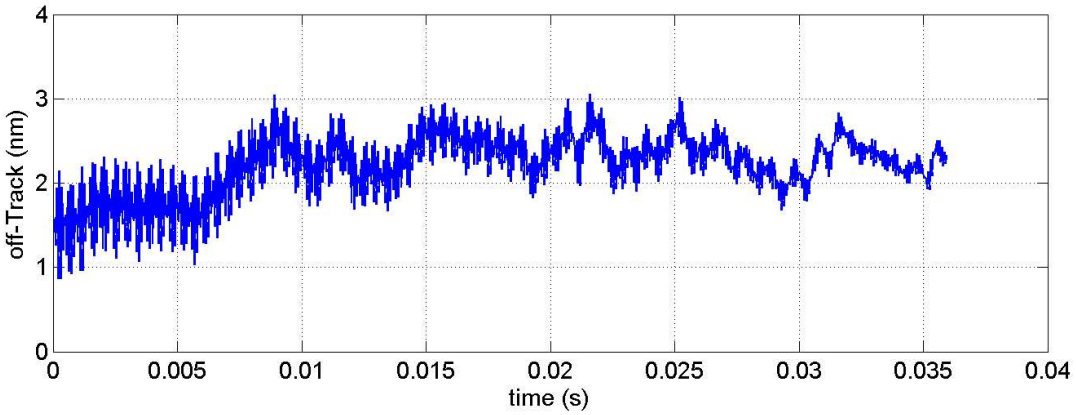

Figure 17: Off-track deflection of arm-tip (nanometers).

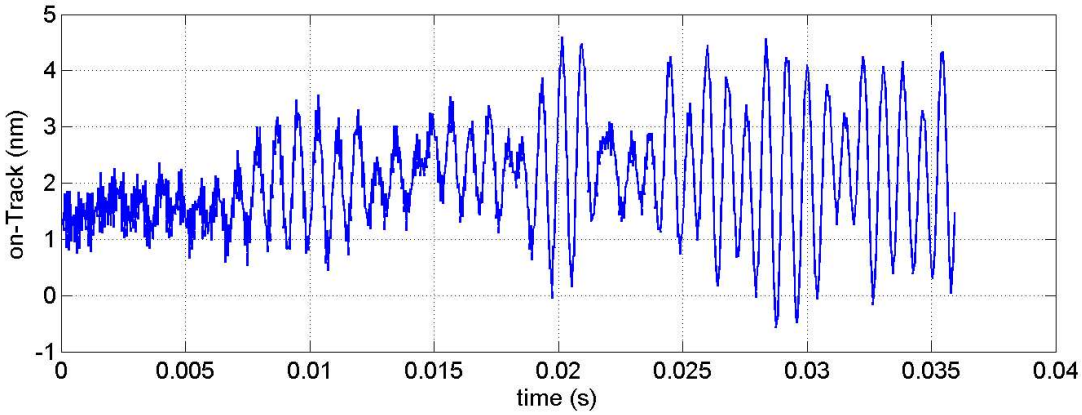

Figure 18: On-track deflection of arm-tip (nanometers).

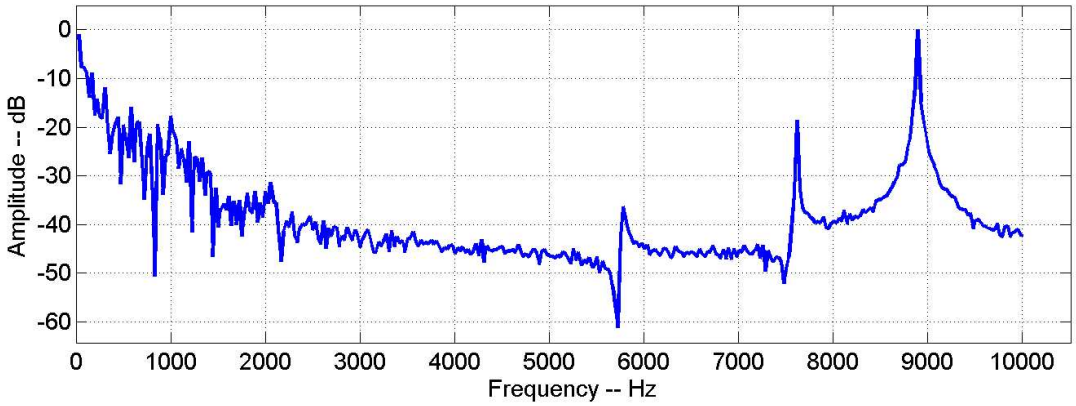

Figure 19: Frequency Spectrum of off-track deflections.

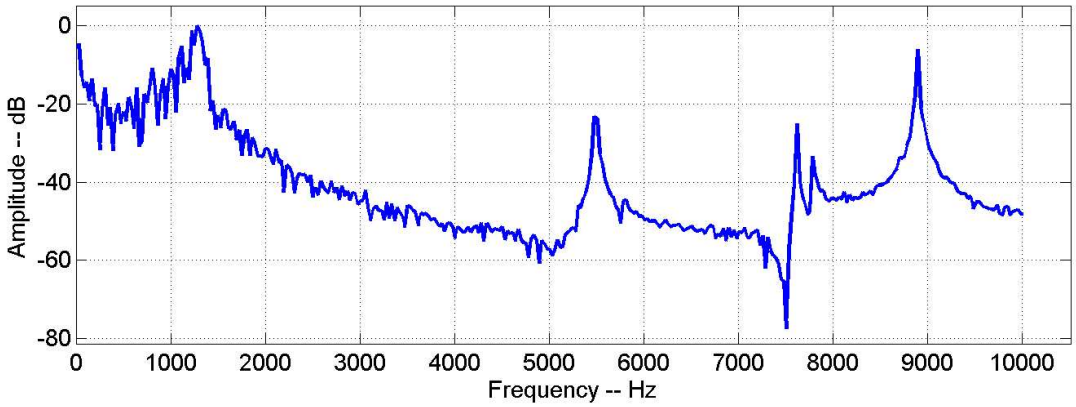

Figure 20: Frequency Spectrum of on-track deflections.

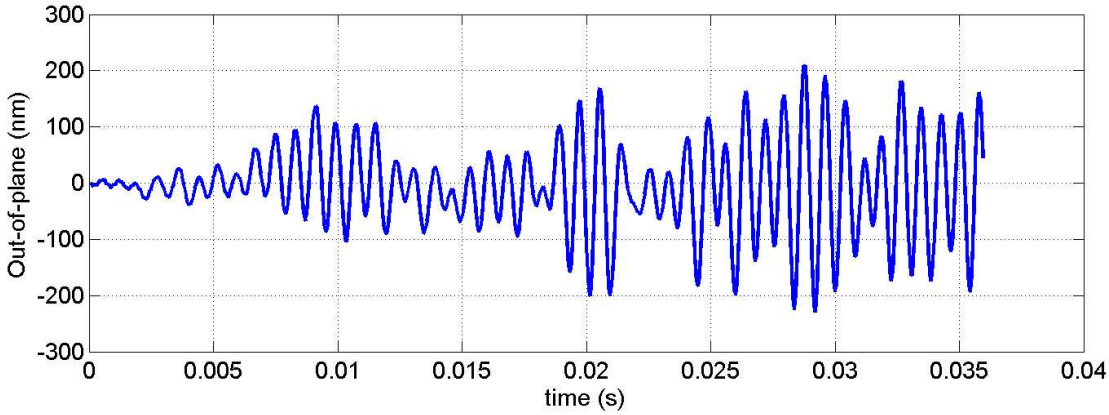

Figure 21: Out of plane (bending) deflections (nanometers).

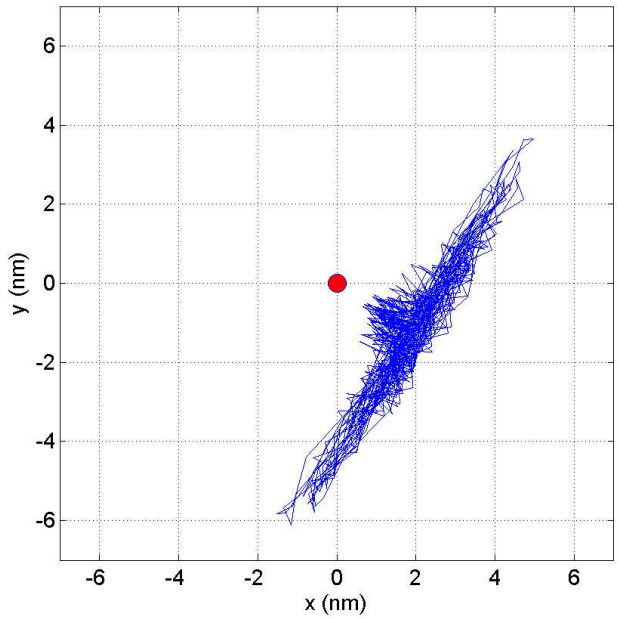

Figure 22: Plot of trajectory of the arm tip in the hortizontal plane.

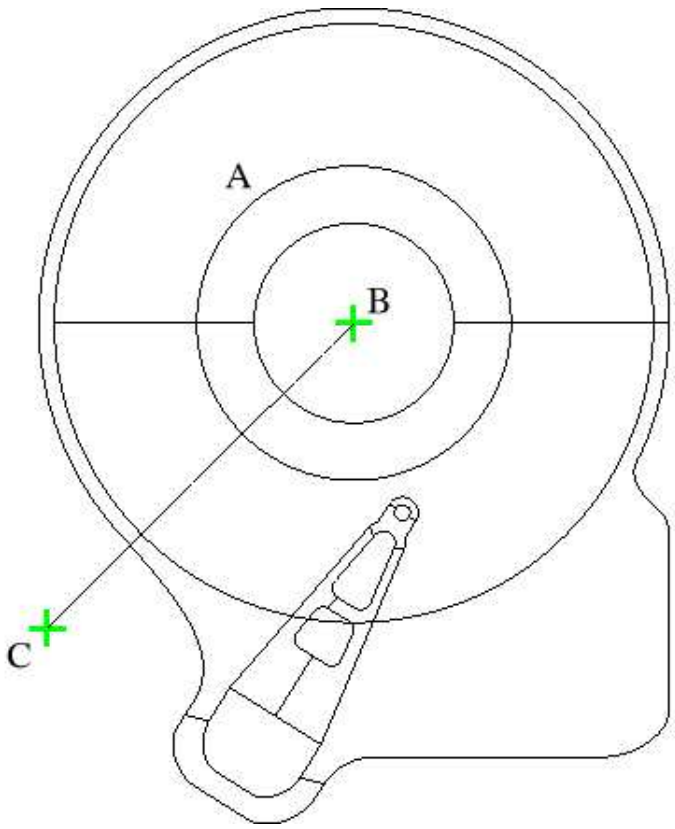

Figure 23: Circle (A) and Radius (B-C) along which comparisons of LES models are made.

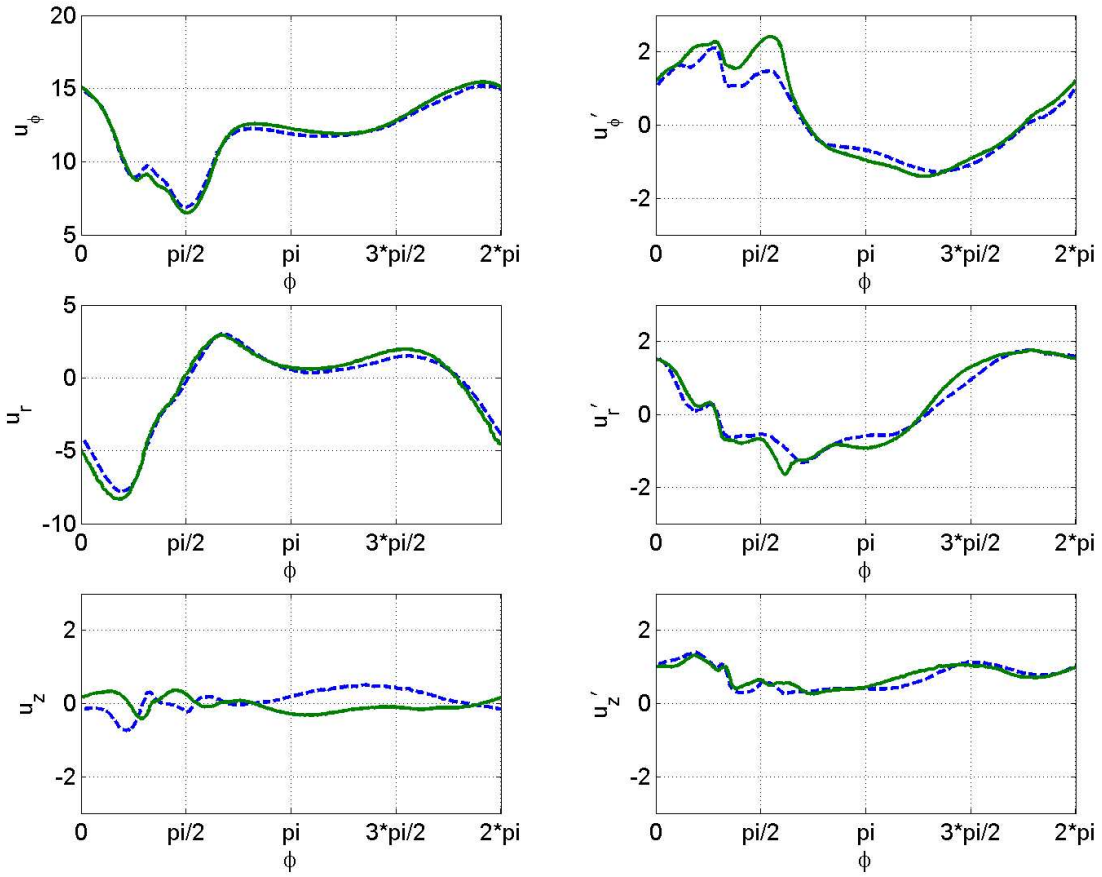

Figure 24: Comparison of velocities predicted by two models along circle A: Dynamic model: full line, Smagorinsky's model: dotted line.

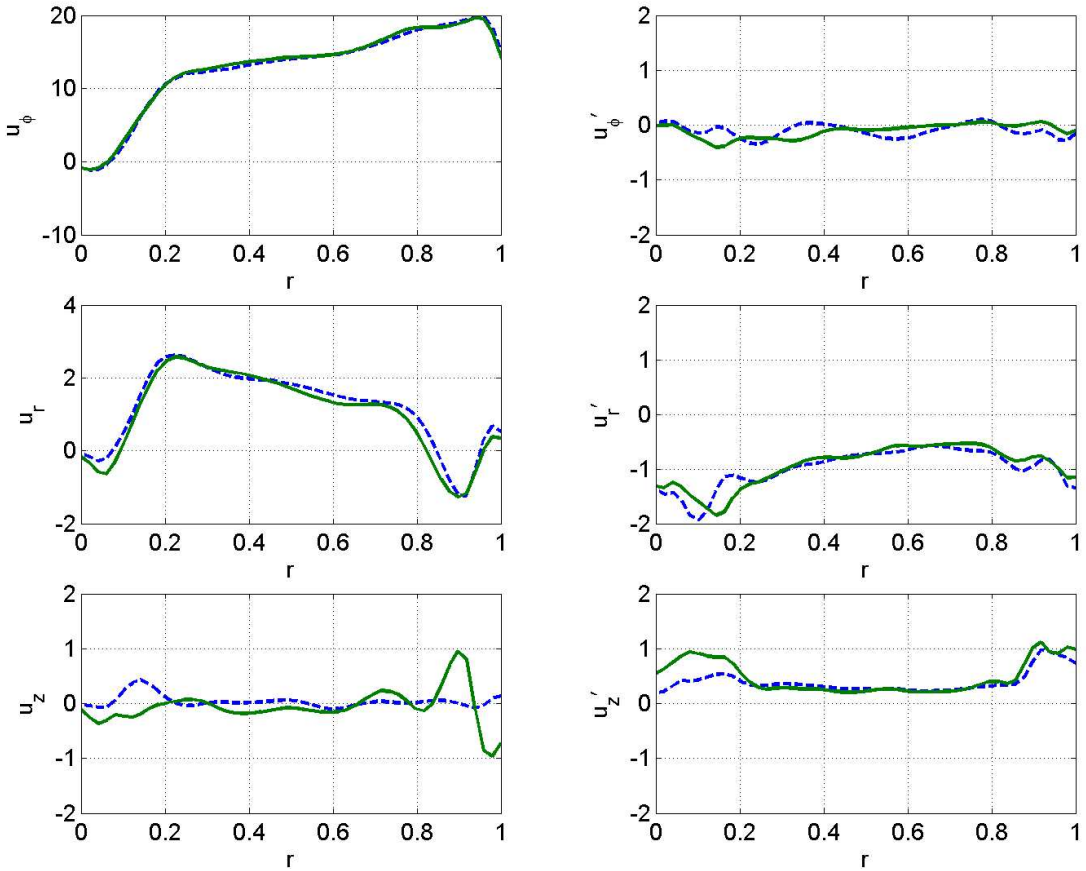

Figure 25: Comparison of velocities predicted by two models along radius B-C: Dynamic model: full line, Smagorinsky's model: dotted line.

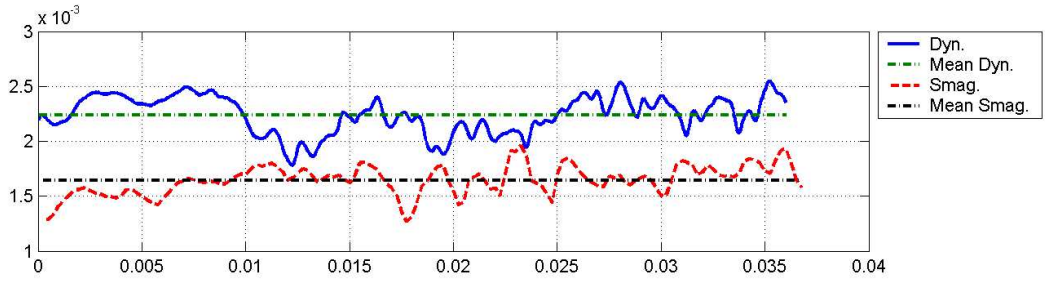

Figure 26: A comparison of pressure drag predicted by both LES models: Observe that the dynamic model predicts higher drag.

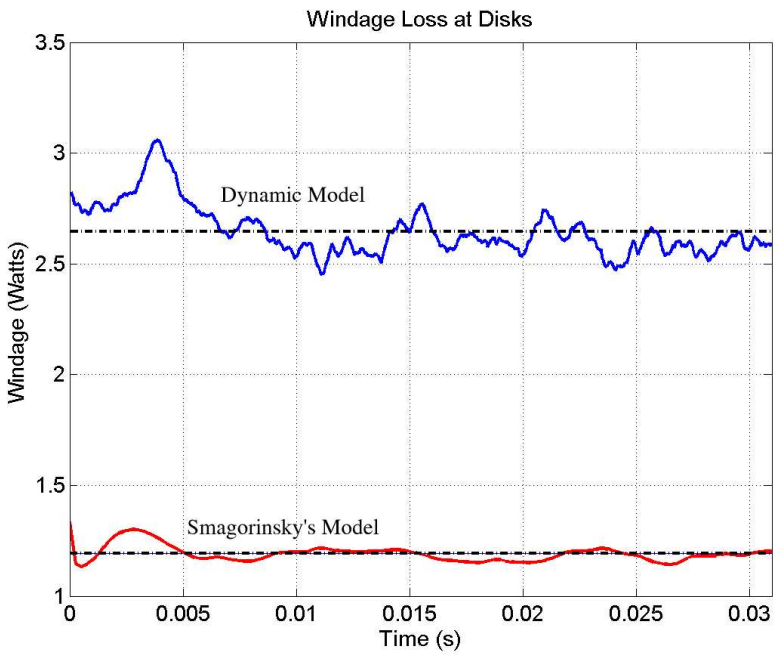

Figure 27: A comparison of windage loss predicted by both LES models: Observe that the dynamic model higher windage.

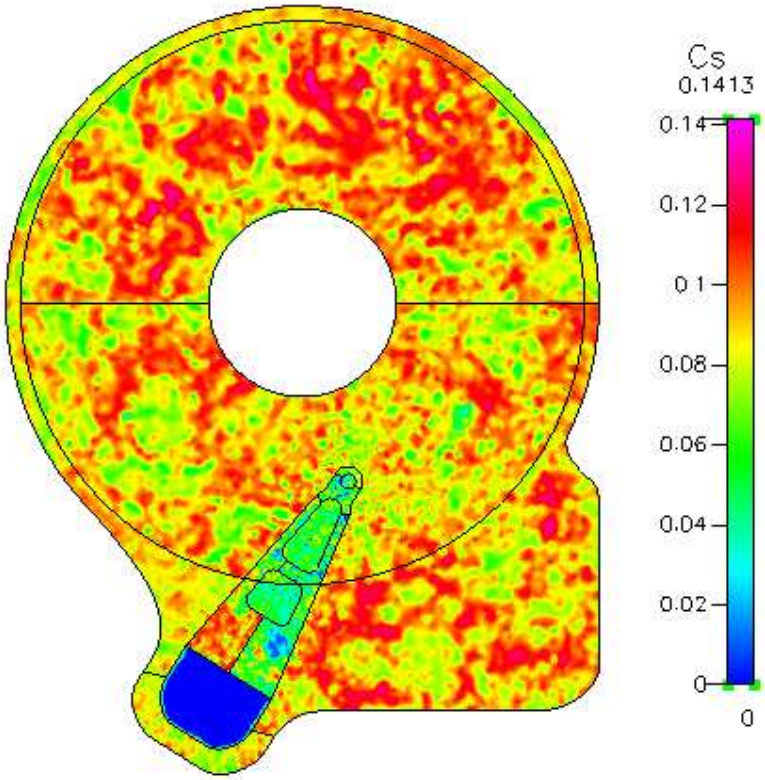

Figure 28: A plot of the dynamic coefficient. Compare to standard value used in the Smagorinsky's model ($C_s = 0.1$)